Poster presentation | Poster session
Poster Session
Thu. Jul 18, 2024 4:30 PM - 6:30 PM Room P

[PO-04] Air–water transport processes of heat and momentum during wind–wave dynamical interactions

*Jinlong Zhang[1], Yuhong Dong[1], Lian Shen[2] (1. Shanghai University, 2. University of Minnesota)

Keywords: turbulence simulation , wind–wave interactions , air/sea interactions

Twelfth International Conference on Computational Fluid Dynamics (ICCFD12), Kobe, Japan, July 14-19, 2024

Air–water transport processes of heat and momentum during wind–wave dynamical interactions

Jinlong Zhang*, Yuhong, Dong*,* and Lian Shen**
Corresponding author: dongyh@shu.edu.cn
* Shanghai Institute of Applied Mathematics and Mechanics, School of Mechanics and Engineering Science, Shanghai Key Laboratory of Mechanics in Energy Engineering and Shanghai Frontier Science Center of Mechanoinformatics, Shanghai University, China.
** Department of Mechanical Engineering and St. Anthony Falls Laboratory, University of Minnesota, USA.

Abstract: Heat and momentum transport processes are studied by direct numerical simulations of air–water two-phase flows with dynamically evolving waves. Three typical cases corresponding to young, intermediate, and old waves are analysed to investigate the roles of wind turbulence and wave motion in the momentum and heat transport processes, which are examined by decomposing the statistics of the airflow and thermal fields into the plane-averaged, wave-induced and turbulent parts. The transport processes of momentum and heat near the interface increasingly differ as the wave age increases. The heat and momentum fluxes exhibit dissimilar phase-dependent variations for turbulent and wave-induced components. Moreover, the competition of wind and waves leads to distinctive differences in momentum and heat fluxes. As the wave age increases, the contribution of the wave-induced component to the total momentum flux increases, while its contribution to the total heat flux decreases. In contrast, the contribution of the turbulence component to the momentum flux decreases, while its contribution to the heat flux increases. Under the coupled wind wave conditions, when the wave age increases, the small-scale intense vortices on the waterside disrupt the overlying flow, further increasing the turbulent heat transfer. However, momentum transfer from the wave to the wind suppresses the downward turbulent momentum transfer.

Keywords: Air/sea interactions, wind–wave interactions, turbulent simulation.

1 Introduction

Air–sea fluxes are fundamentally important in the climate system. The intensity of tropical cyclones depends on air–sea exchanges of heat and momentum. In particular, the air–sea heat flux is a key component of the climate system through which energy flows between the ocean and atmosphere [1]. Hence, investigations of these transport processes in the lower marine atmospheric boundary layer are crucial for weather and marine environment forecasting.

Despite massive efforts to improve the estimation and parameterization of air–sea fluxes, the accurate prediction of air–sea fluxes remains a great challenge. The dependence of the heat and momentum exchange on the wind speed has long been an active research topic [2-4]. In particular, the quantitative relationship between the heat exchange coefficient and wind speed remains controversial according to the results of different experiments [5-7]. This is due to the lack of and differences in field data pertaining to heat fluxes at high wind speeds. Several measurement-based studies have suggested that the momentum exchange coefficient increases with the wind speed under normal conditions, while it tends to level off at extremely high wind speeds. Further understanding some physical processes in air–sea interactions will improve the prediction of air–sea fluxes, for example, the role of ocean surface waves, which are considered to be a key factor and have profound dynamical effects on air–sea fluxes [8,9]. Moreover, wind–wave interactions play important roles in the exchange of heat and momentum across the atmosphere–ocean interface [10]. However, a comprehensive understanding of turbulent processes associated with surface waves is still lacking.

Considering the difficulty of acquiring measurements near the air–sea interface in field observations and laboratory experiments, especially when complex deformations and fractures occur at the interface, numerical simulations have become increasingly useful in obtaining details about the velocity and temperature near the air–sea interface. Previous simulation-based studies have investigated the transport processes of heat and momentum over a wavy surface [11-16]. Surface waves significantly influence the mean flow, turbulent fluxes and coherent structures. To capture the coupling effects between wind and waves in the present study, a direct numerical simulation (DNS) of a two-phase Navier–Stokes equation solver is performed, focusing on turbulent transport processes in coupled air–water flows to investigate the transport characteristics during wind–wave interactions and the roles played by wave and wind turbulence, as this strategy is objectively more advanced than one-fluid models for simulating air–water coupled systems. Previous studies have performed numerical simulations with dynamical tracking of the interface. For example, Lakehal et al. [17] performed DNS to study the effect of a weakly deformed, sheared gas–liquid interface on heat transfer. The influence of variation in low-to-medium Prandtl numbers *Pr* is examined and the scaling of the heat transfer coefficient is derived based on *Pr*. Yamamoto et al. [18] discussed the relationship of turbulent structures with heat transfer. Sensible, latent and radiative heat fluxes were examined by Kurose et al. [19] under the condition of two-phase turbulent flow with a sheared wind-driven gas–liquid interface. The studies so far have obtained a good understanding on the effect of the flows on both sides of the interface on the heat transfer. But the effects of different wind–wave states and their interfacial dynamics have not been fully investigated. Further study on the influence of wind–wave interactions on the air–sea transfer processes is needed to explore the underlying mechanisms.

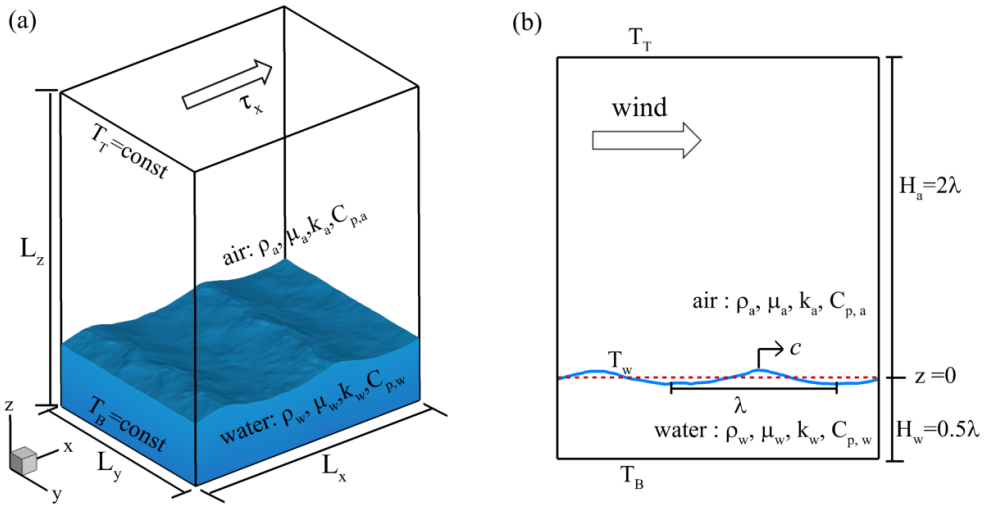

Figure 1: (a) Sketch of the simulation configuration depicting a three-dimensional turbulent flow with air–wave–water interactions. (b) Sketch of the x-z plane: a surface wave with wavelength λ propagates in the x-direction with phase speed c.

2 Problem Statement

The problem considered in the present study is air–water two-phase flows with dynamically evolving waves, where the airflow is fully developed turbulent flow, to investigate the air–sea heat and momentum transport processes by DNS. A sketch of the computational model is shown in figure 1(a). The coordinate used in the present framework is a Cartesian coordinate. The Cartesian coordinates are written as x, y and z, which denote the streamwise, spanwise and vertical directions, respectively, with the corresponding velocity components represented by u, v and w, respectively. The air and water flows are treated as a coherent system, with the density and viscosity varying with the fluid phases. The flow

of the coherent system is driven by a constant streamwise shear stress τ_x, which is imposed on the top boundary. The flow and temperature fields in the air–water system are governed by the following equations:

$$\nabla \cdot \boldsymbol{u} = 0,$$
$$\frac{\partial \boldsymbol{u}}{\partial t} + \boldsymbol{u} \cdot \nabla \boldsymbol{u} = -\frac{1}{\rho(\varphi)} \nabla p + \frac{1}{\rho(\varphi)} \nabla (2\mu(\varphi)\boldsymbol{S}) - \boldsymbol{g},$$
$$\frac{\partial T}{\partial t} + \boldsymbol{u} \cdot \nabla T = \frac{1}{\rho(\varphi) C_p(\varphi)} \nabla \cdot (\kappa(\varphi) \nabla T),$$

where $\rho(\varphi)$ and $\mu(\varphi)$ are the density and viscosity of the fluids, respectively; φ is the level-set (LS) function, which is defined as the signed distance from the air–sea interface, with the sign being positive and negative in water and air, respectively; p is the pressure; $\boldsymbol{S} = (\nabla \boldsymbol{u} + \nabla \boldsymbol{u}^T)/2$ is the strain rate tensor; $\boldsymbol{g}$ is the gravitational acceleration; T is the temperature; $C_p(\varphi)$ is the specific heat at constant pressure; and $\kappa(\varphi)$ is the thermal conductivity.

To perform the two-fluid simulation, an interface-capturing technique is applied. In particular, the coupled level set and volume-of-fluid (CLSVOF) method [20], which combines the level set (LS) method and volume-of-fluid (VOF) method, exhibits good performance in simulations of steep and breaking waves. In the present coherent air–water system, the LS function φ is coupled to the momentum and scalar governing equations through the density ρ, viscosity μ, specific heat C_p and thermal conductivity κ according to

$$\rho(\varphi) = \rho_a + (\rho_w - \rho_a) H(\varphi, \Delta s),$$
$$\mu(\varphi) = \mu_a + (\mu_w - \mu_a) H(\varphi, \Delta s),$$
$$C_p(\varphi) = C_{p,a} + (C_{p,w} - C_{p,a}) H(\varphi, \Delta s),$$
$$\kappa(\varphi) = \kappa_a + (\kappa_w - \kappa_a) H(\varphi, \Delta s),$$

where the subscripts *a* and *w* denote air and water, respectively. The continuous condition across the interface is used for the thermal and velocity fields. To smooth the air–water discontinuity in the computation, the mollified Heaviside function $H(\varphi, \Delta s)$ is used, where $\Delta s = 0.008\lambda$ is the smoothing thickness and λ is the wavelength of the primary wave, as shown in figure 1(b). A more detailed description and validation of the interface tracking method is provided in Liu [21] and Yang et al. [22].

In the simulation of the dynamic evolution of the surface waves, the initial wave geometry is prescribed based on the analytical solution of the third-order Stokes wave. We started our simulation with moderate wave steepness $\varepsilon_0 = a_0 k = 0.25$, a_0 is the initial wave amplitude, where the nonlinear coupling between the wind and waves is stronger compared to the small wave steepness. The wave shape changes over time according to the interactions between the wave and the airflow; however, these waves are not expected to exhibit obvious fragmentation [23-26]. Three typical values for the wave age, namely, $c/u_* = 3.7$, $c/u_* = 12$ and $c/u_* = 27.7$, are chosen based on the findings of previous research [13,15]. The three wave ages chosen are representative of three key stages in wind-wave interactions, corresponding to the young, intermediate and old stages of wind-wave development [27]. As wave age increases, sea states are changed from the young seas to swell conditions. The effects of different wind–wave states and their interfacial dynamics have not been fully investigated before. In the present study, we will explore the influence of wind–wave interactions on the air–sea transfer processes of heat and momentum.

The Reynolds number is set to $Re = \rho_a u_* \lambda / \mu_a = 180$ in the DNS in the present study, which allows the smallest turbulence eddies to be resolved [22,28]. The Prandtl numbers in air and water, $Pr_a = C_{p,a}\mu_a/\kappa_a$ and $Pr_w = C_{p,w}\mu_w/\kappa_w$, for which typical values are chosen to simulate the sensible

heat transfer, are set to 0.71 and 7.38, respectively. The simulation cases and parameters are listed in table 1. In this paper, time t is normalised by the wave period λ/c. The simulation is performed for 20 wave periods, i.e., $t = 0 - 20$. According to the analysis below, the relaxation period of the initial wind–wave interaction is at $t = 0 - 6$. For the statistical results, averaging is performed over the duration $t = 6 - 20$ to obtain converged results. The sampling interval is 0.1, and the total sampling number is 140.

Table 1: List of the computational cases and parameters. Column 1 shows the case identifiers, where the first letter represents the young, intermediate and old waves, and the number represents the wave age 3.7, 12 and 27.7, respectively.

Case	c/u_*	ε_0	Re_a	Pr_a	Pr_w	ρ_a/ρ_w	μ_a/μ_w	κ_a/κ_w	$C_{p,a}/C_{p,w}$
Y037	3.7								
I120	12	0.25	180	0.71	7.38	1.2×10^{-3}	1.54×10^{-2}	3.87×10^{-2}	2.42×10^{-1}
O277	27.7								

Because of the presence of the surface waves, we adopt the triple decomposition approach [29] to analyse the effects of the surface waves on momentum and heat transfer, with the wave-induced contributions quantified. For a variable $f(x,y,z,t)$, the triple decomposition is following

$$f(x,y,z,t) = \overline{f}(z) + \tilde{f}(x,z) + f''(x,y,z,t),$$

where $\overline{f}(z)$ is the plane-averaged components, $\tilde{f}(x,z)$ is the wave-coherent components and $f''(x,y,z,t)$ is the turbulent components. According to the above formulation, the momentum and heat fluxes can be decomposed into the turbulent fluctuation contribution and the wave-coherent contribution. Thus, the momentum flux $\overline{u'w'}$ and heat flux $\overline{\theta'w'}$ consist of the turbulent fluxes ($\overline{u''w''}$ and $\overline{\theta''w''}$) and the wave-induced fluxes ($\overline{\tilde{u}\tilde{w}}$ and $\overline{\tilde{\theta}\tilde{w}}$) as

$$\overline{u'w'} = \overline{u''w''} + \overline{\tilde{u}\tilde{w}},$$

$$\overline{\theta'w'} = \overline{\theta''w''} + \overline{\tilde{\theta}\tilde{w}}.$$

3 Results and discussion

3.1 Evolution of the wind-waves and the flow on the waterside

To illustrate the dynamical processes of the wind–wave interaction, figure 2 shows the evolution of surface waves. After the development of the surface waves enforced by the wind, as expected, the flow has self-adjusted following the early stage of the simulation, as shown in figure 2(a), which illustrates the temporal variation of the wave slope defined as $(\eta_{\max} - \eta_{\min})k/2$, where η is the elevation of the air–sea interface, for the three wave age cases. The initial relaxation stage lasts for approximately 6 wave periods. During these periods, the changes in the wave slope among the three wave ages are similar, all increasing with time. After $t \approx 6$, the amplitude of the wave slope gradually increases with time. This increase arises from the dynamical interaction between the wind and waves. Among the three cases, figure 2(a) shows that the magnitude of wave slope increases more over the same dimensionless time if the wave age is larger. In figure 2(b-d), the wave shape and amplitude are shown by plotting the instantaneous spanwise-averaged wave shape and streamwise gradient at different times. Note that the wave surface is extracted based on the location where the LS function $\varphi = 0$. Overall, the change in the wave shape is small for the three wave age cases. However, the fluctuations in the wave amplitude

increase with increasing wave age, accompanied by a noticeable increase in the wave slope.

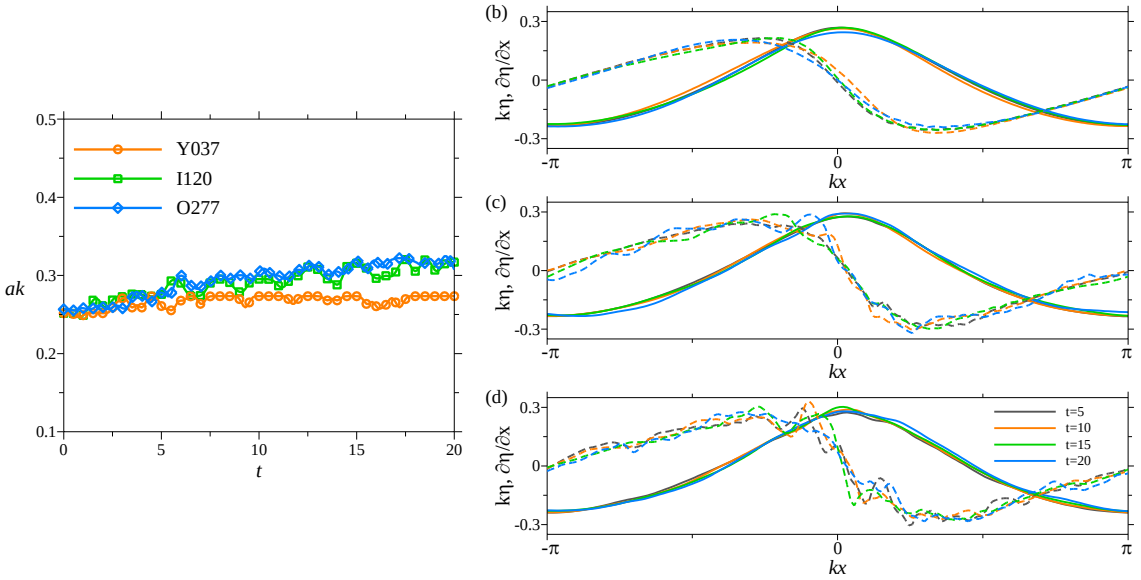

Figure 2: Evolution of the surface waves. (a) Time series of the wave slope ak of the three wave age cases. (b-d) Evolution of the wave shape for cases (b) Y037, (c) I120 and (d) O277. The solid lines show the spanwise-averaged wave shape $\eta(x, t)$, normalised by k, and the dashed lines show its streamwise gradient $\partial\eta(x, t)/\partial x$.

Figure 3 shows the evolution of the spanwise vorticity (defined as $\partial u/\partial z - \partial w/\partial x$) on the waterside at an *x*-*z* plane for cases Y037, I120 and O277. The spanwise vortices on the waterside are enhanced as time increases, and the depth affected by the spanwise vortices increases with time for all cases. However, the large-scale pattern of the spanwise vortices begins to break and the scales of spanwise vortices become smaller with time in cases I120 and O277. The flow structures on the waterside interact with the wind through surface waves and play a role in heat and momentum transfer. We examine the coherent vortical structures in various wind wave states. Previous studies have suggested that coherent vortical structures play important roles in the turbulent heat and momentum transfer processes [15,16,32,33]. Figure 4 displays the coherent vortical structures in cases Y037 and I120, as well as the streamwise vorticity contours, where the Q criterion is used for vortex identification [34], which is defined as

$$Q = \frac{1}{2}\left(\|\boldsymbol{\Omega}\| - \|\boldsymbol{S}\|\right)$$

where $\boldsymbol{\Omega} = (\nabla\boldsymbol{u} - \nabla\boldsymbol{u}^T)/2$ is the rotation rate tensor; $\|\boldsymbol{\Omega}\| = [\mathrm{tr}(\boldsymbol{\Omega}\boldsymbol{\Omega}^T)]^{1/2}$ and $\|\boldsymbol{S}\| = [\mathrm{tr}(\boldsymbol{S}\boldsymbol{S}^T)]^{1/2}$. Because the results in case O277 are similar to those in case I120, case O277 is not shown here. A comparison of figure 4(a) and (b) indicates that the characteristics of the coherent vortical structures differ between cases Y037 and I120. Specifically, the coherent vortical structures are enhanced in case I120, and their scales decrease. This may be associated with the motions on the waterside, where the small-scale intense vortices disrupt the overlying flow. The change in overlying turbulence further affects the heat transfer, which can be seen in section 3.4.

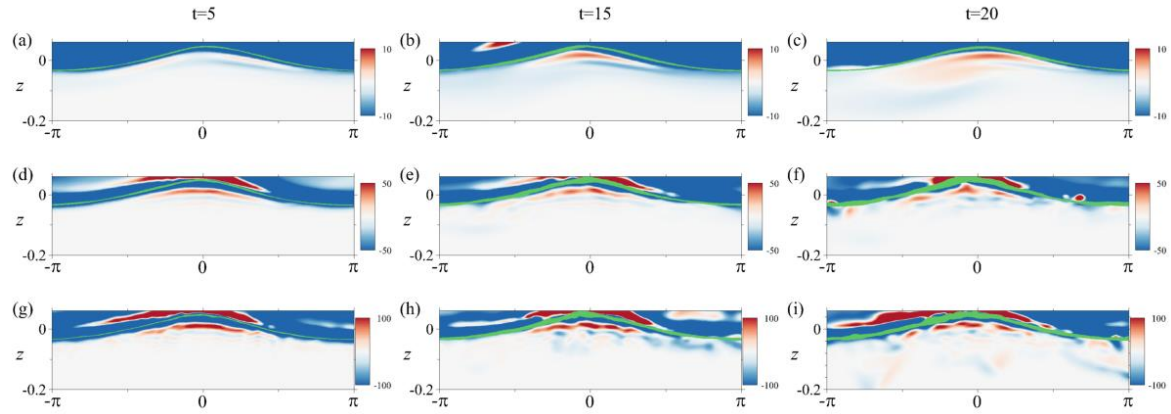

Figure 3: Evolution of the spanwise vorticity on the waterside at an x-z plane for cases (a-c) Y037, (d-f) I120 and (g-i) O277. The green line represents the wave surface.

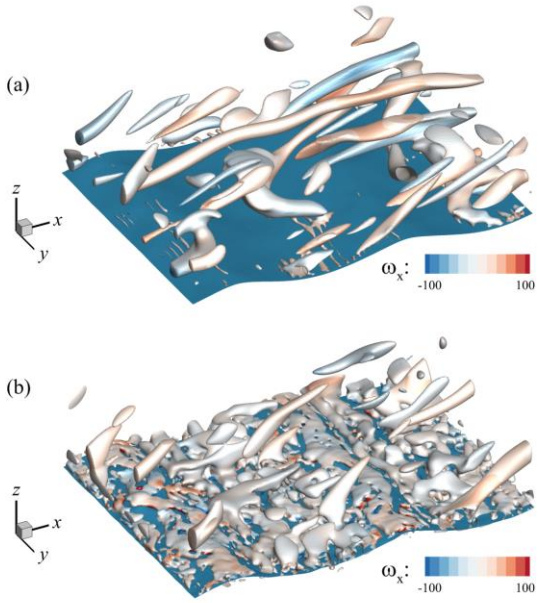

Figure 4: Coherent vortical structures educed by the isosurface of Q = 300 and the streamwise vorticity contours above the wave surface for (a) case Y037 and (b) case I120.

3.2 Wave effects on the mean temperature and velocity

Figure 5 displays the vertical profiles of the plane-averaged temperature $\overline{\theta}$ and streamwise velocity $\overline{u}$. The profiles are plotted in the Cartesian coordinate where the lowest point of the profiles is far away from z = 0. Thus, we can examine the effect of the surface waves on the temperature and velocity fields for various wave age conditions. Note that the velocity is normalised by the friction velocity of the wind turbulence in this paper. Figure 5(a) shows that with increasing wave age, $\overline{\theta}$ decreases slightly near the interface, while $\overline{\theta}$ increases in the region away from the interface (z > 0.12). This is due to the effect of flow structures on the waterside shown in figure 3. The large-scale vortical structures in case Y037 promote the heat transfer across the interface, increasing the surface temperature. Figure 5(b) shows that the value of $\overline{u}$ increases significantly as the wave age increases. In the vicinity of the wave surface, a local minimum in $\overline{u}$ is observed in cases I120 and O277; this could be due to the effect of the positive $\tilde{u}$ near the crest, which accelerates the airflow very close to the wave surface. Due to the local minimum in $\overline{u}$, the streamwise velocity shows a negative vertical gradient near the wave surface. This negative

gradient will suppress the shear production of turbulent momentum flux, thus further reducing the contribution of turbulent momentum flux to momentum transfer.

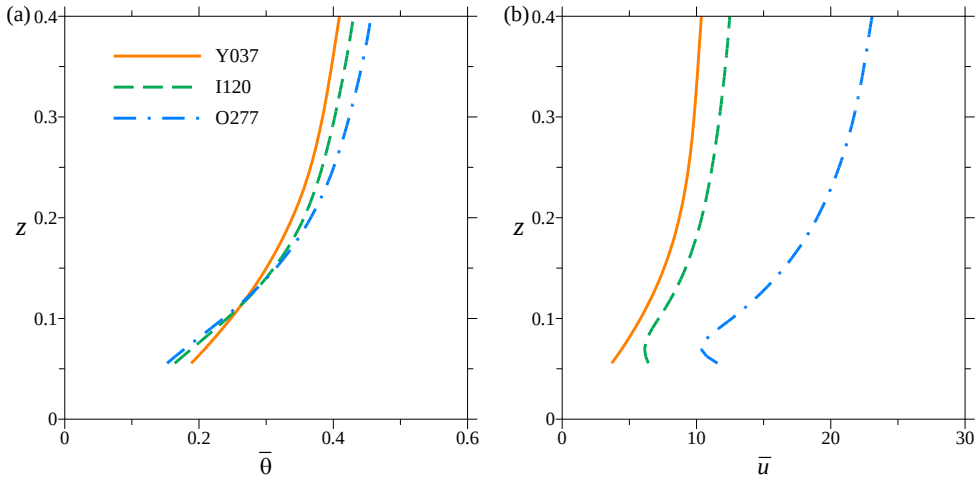

Figure 5: Vertical profiles of the plane-averaged (a) temperature $\overline{\theta}$ and (b) streamwise velocity $\overline{u}$ above the wave crest for various wave age cases.

In addition, the presence of surface waves affects the log-linear profiles. To examine their effect, the von Kármán constant κ_u and roughness length $z^+_{0,u}$ are evaluated from the logarithmic fitting of the profiles of $\overline{u}$, of which the values are listed in table 2. The change in the wave age significantly affects κ_u and $z^+_{0.u}$. The value of κ_u in case O277 is lower than the other two cases. A local acceleration in the velocity in the large wave age case plays a role in the change of the log-linear profile of the velocity. Sullivan et al. [30] also suggested that surface waves with large wave ages cause a discrepancy from the wind profile of the MOST. However, the variation of the von Kármán constant κ_θ and roughness length $z^+_{0,\theta}$ of $\overline{\theta}$ is relatively small.

Table 2: The von Kármán constant κ_u and κ_θ and roughness length $z^+_{0,u}$ and $z^+_{0,\theta}$ obtained from curve fitting of $\overline{u}$ and $\overline{\theta}$ to the logarithmic profiles $\overline{u}^+ = (1/\kappa_u)\ln(z^+/z^+_{0,u})$ and $\overline{\theta}^+ = (1/\kappa_\theta)\ln(z^+/z^+_{0,\theta})$, respectively. The superscript '+' represents the normalisation by the wall units.

Case	κ_u	$z^+_{0,u}$	κ_θ	$z^+_{0,\theta}$
Y037	0.37	1.55	0.33	1.11
I120	0.53	0.10	0.32	0.97
O277	0.18	1.02	0.32	0.72

3.3 Wave-correlated distribution of heat and momentum fluxes

Next, the structures of the turbulent and wave-induced variations in fluxes are examined. The distribution of the phase-averaged wave-induced heat flux $\langle -\tilde{\theta}\tilde{w}\rangle$ is plotted in figure 6. As shown in figure 6(a), $\langle -\tilde{\theta}\tilde{w}\rangle$ is almost always positive over the entire near-surface region in case Y037. In cases I120 and O277, figure 6(b,c) shows that a strong phase-dependent variation is induced by the surface waves, which exhibits an alternating positive–negative pattern along the streamwise direction. The positive maximum of $\langle -\tilde{\theta}\tilde{w}\rangle$ is located leeward of the wave crest, while its negative maximum is observed windward of the wave crest (see figure 6b,c). Moreover, figure 6(a-c) shows that the maximum

intensity of $\langle -\tilde{\theta}\tilde{w} \rangle$ increases as the wave age increases.

The vertical profiles of the plane-averaged wave-induced heat flux $-\overline{\tilde{\theta}\tilde{w}}$ are shown in figure 6(d-f). The value of $-\overline{\tilde{\theta}\tilde{w}}$ near the wave surface is lower in cases I120 and O277 than in case Y037, which is caused by the offset from the alternating positive–negative pattern of $\langle -\tilde{\theta}\tilde{w} \rangle$ occurring in the larger wave age cases. Figure 6(b,c) also shows that the positive and negative $\langle -\tilde{\theta}\tilde{w} \rangle$ intensities are asymmetric along the wave surface, and the positive $\langle -\tilde{\theta}\tilde{w} \rangle$ is more intense. As a result, the sign of $-\overline{\tilde{\theta}\tilde{w}}$ is positive near the wave surface, indicating that the overall wave-induced variation in the heat flux is directed downward towards the wave surface, as shown in figure 6(e,f).

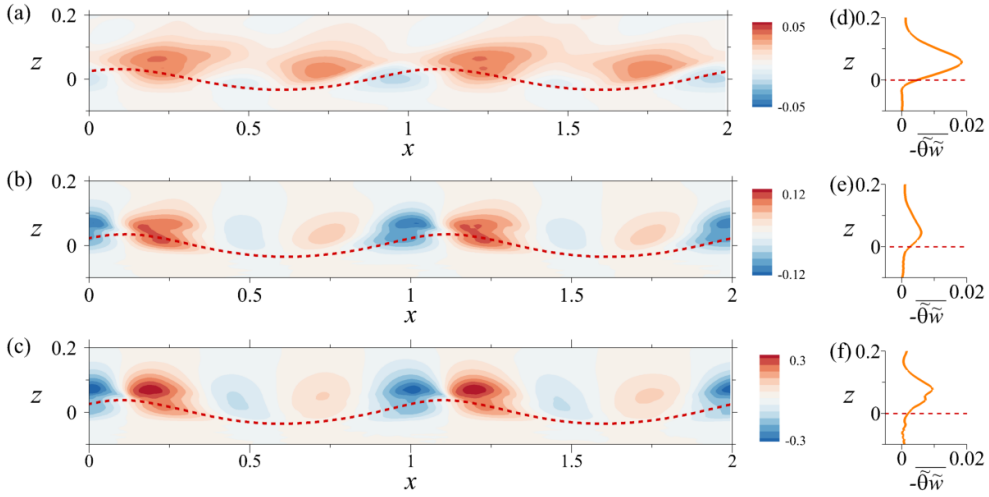

Figure 6: Phase-averaged contours of the wave-induced heat flux over the wave surface, $\langle -\tilde{\theta}\tilde{w} \rangle$, for different wave age cases: (a) Y037; (b) I120; and (c) O277. (d-f) The corresponding profiles of the plane-averaged wave-induced heat flux $-\overline{\tilde{\theta}\tilde{w}}$ in cases Y037, I120 and O277. The red dashed line represents the mean wave surface.

Figure 7 shows the contours of the wave-induced momentum flux $\langle -\tilde{u}\tilde{w} \rangle$. Figure 7(a-c) demonstrates that the alternating positive–negative pattern of $\langle -\tilde{u}\tilde{w} \rangle$ is more obvious in the larger wave age cases of I120 and O277 than in case Y037, and the magnitude of the positive $\langle -\tilde{u}\tilde{w} \rangle$ on the leeward side is slightly higher than that of the negative $\langle -\tilde{u}\tilde{w} \rangle$ on the windward side. This distribution appears different from the laboratory result of Yousefi et al. [31] where negative $\langle -\tilde{u}\tilde{w} \rangle$ is not found on the windward side. This discrepancy is due to the use of different coordinate systems, as reported by Yousefi et al. [31]. In case Y037, the wave-induced momentum flux is almost entirely positive, which indicates momentum transfer in the downward direction, near the wave surface (figure 7a). Compared to the structure of $\langle -\tilde{\theta}\tilde{w} \rangle$, the structure of $\langle -\tilde{u}\tilde{w} \rangle$ is stretched along the surface waves, and thus, the vertical region affected by the wave-induced momentum flux is smaller than the region affected by the wave-induced heat flux. This phenomenon can also be further observed in figure 7(d-f), in which the profiles of the plane-averaged wave-induced momentum flux $-\overline{\tilde{u}\tilde{w}}$ are plotted. The magnitude of $-\overline{\tilde{u}\tilde{w}}$ decreases rapidly as the distance from the wave surface increases, and $-\overline{\tilde{u}\tilde{w}}$ is approximately zero above the height of $z = 0.1$. In comparison, $-\overline{\tilde{\theta}\tilde{w}}$ is still relatively high at a height of $z = 0.1$ and decreases to a near-zero magnitude near $z = 0.2$ (see figure 6d-f).

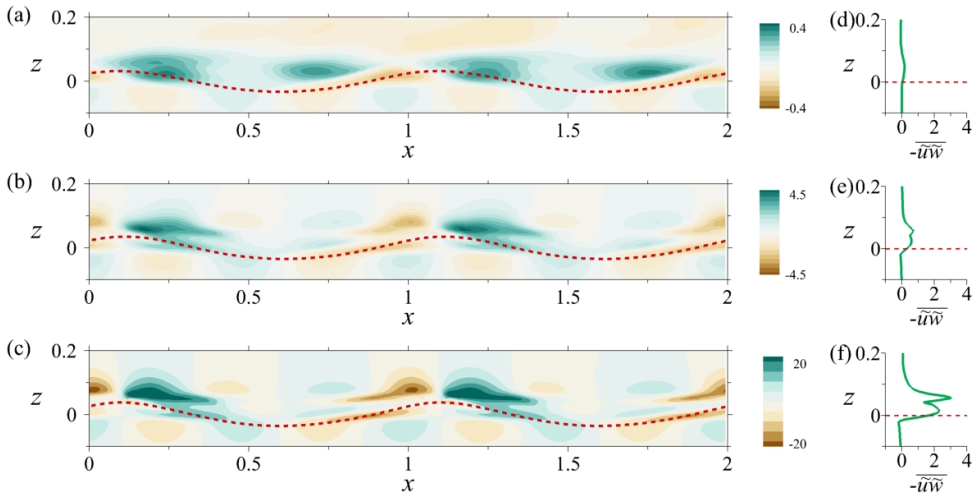

Figure 7: Phase-averaged contours of the wave-induced momentum flux over the wave surface, $\langle -\tilde{u}\tilde{w}\rangle$, for different wave age cases: (a) Y037; (b) I120; and (c) O277. (d-f) The corresponding profiles of the plane-averaged wave-induced momentum flux $-\overline{\tilde{u}\tilde{w}}$ in cases Y037, I120 and O277. The red dashed line represents the mean wave surface.

The distribution of the phase-averaged turbulent heat flux $\langle -\theta''w''\rangle$ is displayed in figure 8(a-c). Figure 8(a) shows that $\langle -\theta''w''\rangle$ exhibits an obvious layer near the wave surface, where its magnitude is very weak, in case Y037. As the wave age increases, the magnitude of $\langle -\theta''w''\rangle$ near the wave surface increases and exhibits a phase-dependent variation, as shown in figure 8(b,c). Similar wave-correlated variations in $\langle -\theta''w''\rangle$ were also suggested to occur in the larger wave age cases by Yang & Shen [16], but the variations were confined to the region immediately adjacent to the wave surface. The results of the present study indicate that fully coupled wind waves affect the near-surface motions, further changing the structure of the turbulent heat flux. In addition, figure 8(b,c) shows that the region of negative $\langle -\theta''w''\rangle$ is located on the windward side of the wave crest for cases I120 and O277. The negative $\langle -\theta''w''\rangle$ is caused by the positive vertical gradients of $\langle w\rangle$ on the windward side, which leads to the same signs of θ'' and w''. In case Y037, the vertical gradient gradient of $\langle w\rangle$ is negative on the windward side, which are not shown. Above this region, $\langle -\theta''w''\rangle$ is positive and less dependent on the wave phase. In case Y037, the negative $\langle -\theta''w''\rangle$ region is insignificant. In addition, the correlation between the flux isolines and the wave phase is not obvious, as shown in figure 8(a). Figure 8(c) shows that there is a thin layer of positive $\langle -\theta''w''\rangle$ near the wave surface in case O277, which is absent in cases Y037 and I120. This phenomenon is associated with the effect of waterside motions on the overflying flow.

Figure 8(d-f) shows the profiles of the plane-averaged turbulent heat flux $-\overline{\theta''w''}$. Figure 8(d) shows that $-\overline{\theta''w''}$ is approximately zero up to the height of $z \approx 0.07$ in case Y037. This is due to the existence of a weak $-\overline{\theta''w''}$ layer where the flux isolines are independent of the wave phase, as reported in figure 8(a). Above this height, $-\overline{\theta''w''}$ increases rapidly with increasing distance from the wave surface. In cases I120 and O277, $-\overline{\theta''w''}$ decreases gradually as the distance from the wave surface decreases, as shown in figure 8(e,f). This decrease is caused by the alternating positive–negative pattern of $\langle -\theta''w''\rangle$ near the wave surface, as shown in figure 8(b,c). Furthermore, the reduction in the turbulent heat flux adjacent to the surface in case Y037 indicates that the turbulent effect on the heat transfer process is suppressed near the wave surface. The effect of the diffusive heat transfer can be enhanced. However, in the larger wave age cases, the turbulence effect is increased.

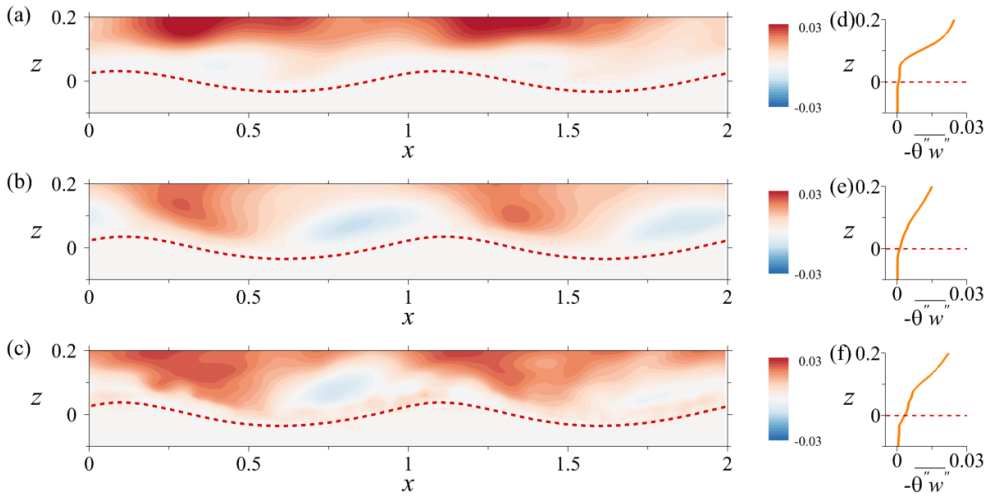

Figure 8: Phase-averaged contours of the turbulent heat flux over the wave surface, $\langle -\theta''w''\rangle$, for different wave age cases: (a) Y037; (b) I120; and (c) O277. (d-f) The corresponding profiles of the plane-averaged turbulent heat flux $-\overline{\theta''w''}$ in cases Y037, I120 and O277. The red dashed line represents the mean wave surface.

The contours of the phase-averaged turbulent momentum flux $\langle -u''w''\rangle$ are displayed in figure 9(a-c). The phase dependence of $\langle -u''w''\rangle$ near the wave surface becomes more apparent with increasing wave age. Despite the difference in the sign caused by the different reference frames pointed out above, the characteristics of asymmetry in the intensity of $\langle -u''w''\rangle$ are similar to the observation of Yousefi et al. [31], with more intense $\langle -u''w''\rangle$ on the leeward side of the wave crest than the windward side. Figure 9(a) shows that the magnitude of $\langle -u''w''\rangle$ increases gradually as the distance from the wave surface increases in case Y037. In contrast, in the larger wave age cases, the maximum $\langle -u''w''\rangle$ occurs in a thin layer near the wave crest, which is particularly apparent in case O277, as shown in figure 9(b,c). This phenomenon reflects the momentum exchange between the wave-induced perturbation and background turbulence, indicating that the turbulent component $\langle -u''w''\rangle$ is significantly affected by the wave-induced motions in the larger wave age cases. A comparison of figures 8(a-c) and 9(a-c) suggests that this phenomenon does not exist for $\langle -\theta''w''\rangle$.

In addition, figure 9(d-f) shows the profiles of the plane-averaged turbulent momentum flux $-\overline{u''w''}$. The profile of $-\overline{u''w''}$ exhibits a local maximum close to the wave surface in cases I120 and O277, as shown in figure 9(e,f). This is associated with the local maximum $\langle -u''w''\rangle$ in the region adjacent to the wave surface observed in figure 9(b,c). A comparison of the results in figures 8(d) and 9(d) suggests that the behaviours of $-\overline{u''w''}$ and $-\overline{\theta''w''}$ differ near the wave surface in case Y037. Figure 9(d) shows that $-\overline{u''w''}$ decreases gradually with decreasing distance from the wave surface, and a region with a near-zero value is not observed. The undulation of the surface waves is responsible for this phenomenon.

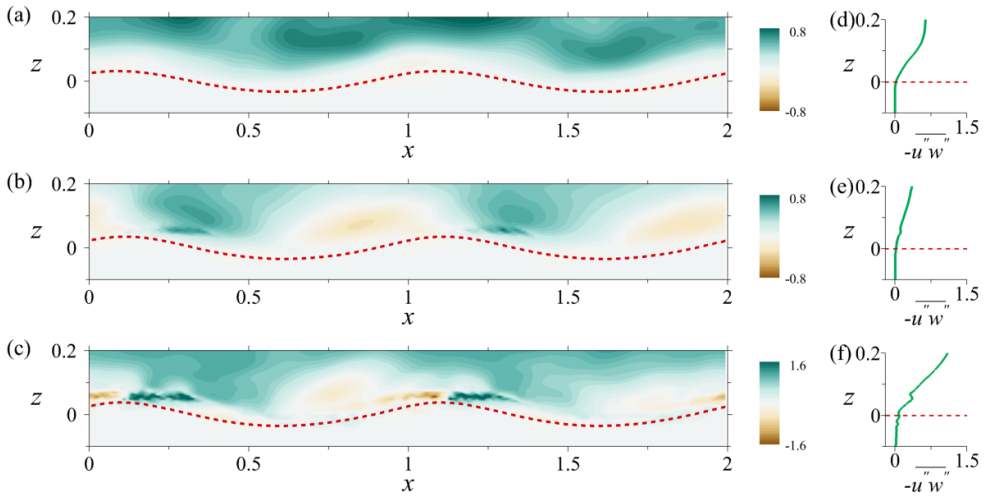

Figure 9: Phase-averaged contours of the turbulent momentum flux over the wave surface, $\langle -u''w'' \rangle$, for different wave age cases: (a) Y037; (b) I120; and (c) O277. (d-f) The corresponding profiles of the plane-averaged turbulent momentum flux $-\overline{u''w''}$ in cases Y037, I120 and O277. The red dashed line represents the mean wave surface.

3.4 Role of surface waves in heat and momentum transfer

The profiles of the plane-averaged turbulent heat flux $-\overline{\theta''w''}$ and turbulent momentum flux $-\overline{u''w''}$ are plotted in figure 10 together with the profiles of the corresponding plane-averaged total fluxes $-\overline{\theta'w'}$ and $-\overline{u'w'}$, for the various wave age cases. The turbulent heat and momentum fluxes both increase gradually with increasing altitude and approach constant values far from the wave surface. Moreover, both fluxes decrease rapidly near the wave surface, as shown in figure 10. This behaviour is due to the restriction of the wave surface on the turbulent fluctuations and the viscous effect near the wave surface. A comparison of the total flux and turbulent flux near the surface reveals an obvious difference among the three cases. For heat fluxes, near the wave surface, the contribution of $-\overline{\theta''w''}$ to $-\overline{\theta'w'}$ is relatively low in case Y037, while the contribution of $-\overline{\theta''w''}$ increases in cases I120 and O277, as shown in figure 10(a-c). This indicates that the effects of turbulent motions on heat transfer are enhanced as the wave age increases, corresponding to the increasing role of turbulent heat transfer. In contrast, figure 10(d-f) shows that $-\overline{u''w''}$ has a larger contribution to $-\overline{u'w'}$ in case Y037, but its contribution dramatically decreases in cases I120 and O277. The above differences between the total fluxes and the turbulent flux components indicate that the wave-induced contributions to fluxes cannot be ignored. For the larger wave age cases, the contribution of the wave-coherent motions leads to a significant increase in the momentum flux, as shown in figure 10(e,f). Far from the wave surface, this difference diminishes: in this region, the turbulent fluxes are nearly equal to the total fluxes, and the wave-induced contributions are negligible. These qualitatively opposite trends indicate the inconsistent responses to surface waves for heat and momentum transfer processes near the wave surface.

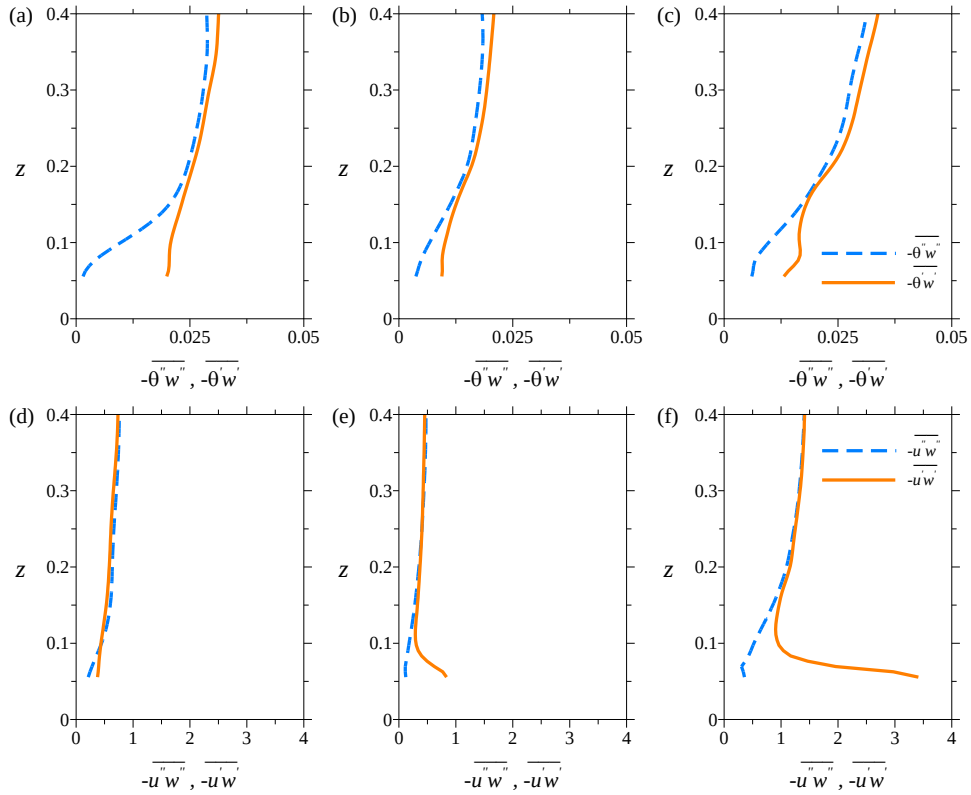

Figure 10: Vertical profiles of the plane-averaged heat and momentum fluxes: (a-c) heat flux and (d-f) momentum flux. The turbulent fluxes $-\overline{\theta''w''}$ and $-\overline{u''w''}$ and total fluxes $-\overline{\theta'w'}$ and $-\overline{u'w'}$ are also shown to analyse the effects of surface waves on the heat and momentum fluxes, for various wave age cases: (a,d) Y037; (b,e) I120; (c,f) O277.

The quadrant analysis is further used to examine the effect of ejection and sweep motions on the turbulent heat and momentum transfer processes, which is a useful tool for understanding the flow physics of the production of turbulent fluxes [35,36]. The contributions to the turbulent heat flux $\theta''w''$ and turbulent momentum flux $u''w''$ are divided into four quadrants: $Q1\left((u''(\theta'')>0, w''>0)\right)$, $Q2\left((u''(\theta'')<0, w''>0)\right)$, $Q3\left((u''(\theta'')<0, w''<0)\right)$, and $Q4\left((u''(\theta'')>0, w''<0)\right)$. Here, $Q2$ and $Q4$ correspond to ejections and sweeps, respectively, which are essential for the downward fluxes, whereas $Q1$ and $Q3$ represent the upward turbulent fluxes. Previous studies have suggested that the $Q2$ and $Q4$ motions are the principal mechanisms underlying downward turbulent fluxes [33].

Figure 11 shows the ratio $-(Q2 + Q4)/(Q1 + Q3)$ between quadrants as a function of the wave age for $\theta''w''$ and $u''w''$, which represents the relative importance of the downward and upward fluxes. To illustrate the role of coupled wind waves in heat and momentum transfer, a simulation of prescribed surface waves is conducted and their results are compared in figure 11. For turbulent heat transfer, when the wave age increases, an opposite trend between coupled wind waves and prescribed surface waves is observed (see figure 11a). The ratio in the coupled wind waves increases with the wave age, while the ratio of prescribed surface waves decreases with the wave age. For the turbulent momentum flux, the trend of -($Q2$+$Q4$)/($Q1$+$Q3$) is similar between coupled wind waves and prescribed wind waves, as shown in figure 11(b). Their different responses to the wind–wave coupling lead to the dissimilar contribution of turbulent fluxes with wave ages.

In addition, figure 11(b) shows that the ratio of $u''w''$ in case Y037 is remarkably larger than that in cases I120 and O277, indicating that the stronger ejections and sweeps occur in case Y037 than in

the larger wave ages. The momentum transfer from the waves to the wind contributes to the smaller ratio in the larger wave age cases. Figure 12 shows the vertical profiles of the skewness of w''. $S(w'')$ is negative in case Y037, whereas $S(w'')$ is positive near the wave surface in cases I120 and O277. The negative $S(w'')$ indicates that w'' is mainly associated with the strong downward motions that lead to the negative w'' in case Y037. In contrast, the positive $S(w'')$ reflects that w'' is primarily influenced by strong upward motions in larger wave age cases. This increasing importance of upward motions correlates with the strong modulation effect of the waves on the wind turbulence. Thus, momentum transfer from the waves to the wind occurs in the larger wave age cases, which was also reported by Grachev & Fairall [37] and Sullivan et al. [38].

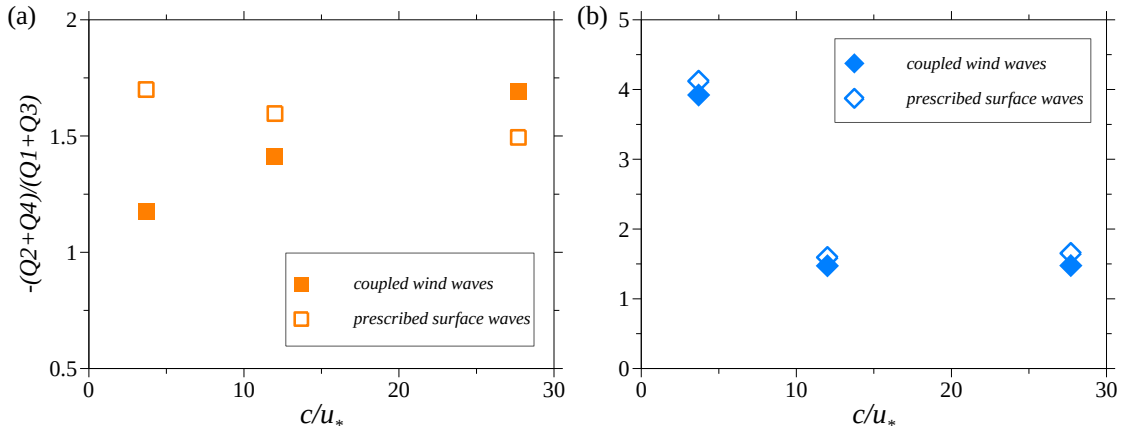

Figure 11: Comparison of quadrant analysis of the (a) turbulent heat flux $\theta''w''$ and (b) turbulent momentum flux $u''w''$ between coupled wind waves and prescribed surface waves as a function of the wave age at the horizontal plane of $z = 0.06$.

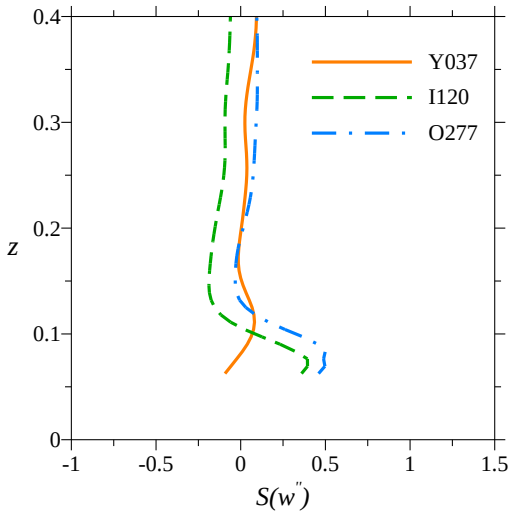

Figure 12: Comparison of the profiles of skewness in various wave age cases for the turbulent vertical velocity fluctuation w''.

4 Conclusion

By simulating the dynamic water surface influenced by wind–wave interactions and the processes of momentum and heat transport across the interface, the effects of turbulent wind and wave motions on the flow and thermal fields are examined. The dissimilar transport behaviour of heat and momentum

near the wave surface is elucidated, which is linked to the effect of the wave age on wind–wave interactions. The different wave-correlated distributions are responsible for the distinct behaviours between heat and momentum transfer. The transport efficiency of heat increases with the wave age, while the transport efficiency of momentum decreases with the wave age. When the wave age increases, the momentum transfer from the waves to the wind occurs, and the near-surface wave-driven jet is generated, accompanied by the enhancement of turbulence close to the wave surface. The turbulent heat and momentum transfer exhibit different responses to this effect of wind–wave coupling. Upward momentum transfer weakens the turbulence contribution to momentum transfer. In contrast, the turbulence enhanced by the waterside motions increases the turbulent heat transfer. As another component, the contribution of wave-induced components to total heat and momentum fluxes changes accordingly.

References

[1] B. P. Kumar, M. F. Cronin, S. Joseph, M. Ravichandran & N. Sureshkumar. Latent heat flux sensitivity to sea surface temperature: regional perspectives. J. Clim., 30 (1): 129–143, 2017.

[2] C. W. Fairall, E. F. Bradley, J. E. Hare, A. A. Grachev & J. B. Edson. Bulk parameterization of air–sea fluxes: updates and verification for the COARE algorithm. J. Clim., 16 (4): 571–591, 2003.

[3] D. Jeong, B. K. Haus & M. A. Donelan. Enthalpy transfer across the air–water interface in high winds including spray. J. Atmos. Sci., 69 (9): 2733–2748, 2012.

[4] Y. Troitskaya, D. Sergeev, M. Vdovin, A. Kandaurov, O. Ermakova & N. Takagaki. A laboratory study of the effect of surface waves on heat and momentum transfer at high wind speeds. J. Geophys. Res. Oceans, 125 (7): e2020JC016276, 2020.

[5] E. L. Andreas & J. Decosmo. The signature of sea spray in the HEXOS turbulent heat flux data. Boundary-Layer Meteorol., 103 (2): 303–333, 2002.

[6] W. M. Drennan, J. A. Zhang, J. R. French, C. McCormick & P. G. Black. Turbulent fluxes in the hurricane boundary layer. Part II: Latent heat flux. J. Atmos. Sci., 64 (4): 1103–1115, 2007.

[7] S. Komori, K. Iwano, N. Takagaki, R. Onishi, R. Kurose, K. Takahashi & N. Suzuki. Laboratory measurements of heat transfer and drag coefficients at extremely high wind speeds. J. Phys. Oceanogr., 48 (4): 959–974, 2018.

[8] L. Cavaleri, B. Fox-Kemper and M. Hemer. Wind waves in the coupled climate system. Bull. Amer. Meteor. Soc., 93:1651–1661, 2012.

[9] A. V. Babanin. Ocean waves in large-scale air-sea weather and climate systems. J. Geophys. Res. Oceans, 128:e2023JC019633, 2023.

[10] B. Zhao, G. Wang, J. A. Zhang, L. Liu, J. Liu, J. Xu, et al. The effects of ocean surface waves on tropical cyclone intensity: Numerical simulations using a regional atmosphere-ocean-wave coupled model. J. Geophys. Res. Oceans, 127:e2022JC019015, 2022.

[11] N. Kihara, H. Hanazaki, T. Mizuya & H. Ueda. Relationship between airflow at the critical height and momentum transfer to the traveling waves. Phys. Fluids, 19 (1): 015102, 2007.

[12] T. Hara & P. P. Sullivan. Wave boundary layer turbulence over surface waves in a strongly forced condition. J. Phys. Oceanogr., 45 (3): 868–883, 2015.

[13] P. P. Sullivan, J. C. McWilliams & C. H. Moeng. Simulation of turbulent flow over idealized water waves. J. Fluid Mech., 404: 47–85, 2000.

[14] D. Yang & L. Shen. Characteristics of coherent vortical structures in turbulent flows over progressive surface waves. Phys. Fluids, 21 (12): 125106, 2009.

[15] D. Yang & L. Shen. Direct-simulation-based study of turbulent flow over various waving boundaries. J. Fluid Mech., 650: 131–180, 2010.

[16] D. Yang & L. Shen. Direct numerical simulation of scalar transport in turbulent flows over progressive surface waves. J. Fluid Mech., 819: 58–103, 2017.

[17] D. Lakehal, M. Fulgosi, G. Yadigaroglu & S. Banerjee. Direct numerical simulation of turbulent heat transfer across a mobile, sheared gas–liquid interface. ASME J. Heat Transfer, 125 (6): 1129–1139, 2003.

[18]Y. Yamamoto, T. Kunugi, S. Satake & A. Serizawa. Turbulent structures and heat transfer across the air-liquid interface in the wind-driven turbulent flow. Trans. JSME B, 70 (692): 1006–1012, 2004.
[19]R. Kurose, N. Takagaki, A. Kimura & S. Komori. Direct numerical simulation of turbulent heat transfer across a sheared wind-driven gas–liquid interface. J. Fluid Mech., 804: 646–687, 2016.
[20]M. Sussman and E. G. Puckett. A coupled level set and volume-of-fluid method for computing 3D and axisymmetric incompressible two-phase flows. J. Comput. Phys., 162 (2):301–337, 2000.
[21]Y. Liu. Numerical study of strong free surface flow and breaking waves. PhD thesis, The Johns Hopkins University, 2012.
[22]Z. X. Yang, B. Q. Deng and L. Shen. Direct numerical simulation of wind turbulence over breaking waves. J. Fluid Mech., 850:120–155, 2018.
[23]A. Iafrati. Numerical study of the effects of the breaking intensity on wave breaking flows. J. Fluid Mech., 622: 371–411, 2009.
[24]L. Deike, S. Popinet & W. K. Melville. Capillary effects on wave breaking. J. Fluid Mech., 769: 541–569, 2015.
[25]S. D. Giorgio, S. Pirozzoli & A. Iafrati. On coherent vortical structures in wave breaking. J. Fluid Mech., 947: A44, 2022.
[26]J. Wu, S. Popinet & L. Deike. Revisiting wind wave growth with fully coupled direct numerical simulations. J. Fluid Mech., 951: A18, 2022.
[27]S. E. Belcher & J. C. R. Hunt. Turbulent flow over hills and waves. Annu. Rev. Fluid Mech., 30 (1): 507–538, 1998.
[28]S. Tang, Z. X. Yang, C. X. Liu, Y. H. Dong & L. Shen. Numerical study on the generation and transport of spume droplets in wind over breaking waves. Atmosphere, 8 (12): 248, 2017.
[29]A. K. M. F. Hussain & W. C. Reynolds. The mechanics of an organized wave in turbulent shear flow. J. Fluid Mech., 41 (2): 241–258, 1970.
[30]P. P. Sullivan, J. C. McWilliams & E. G. Patton. Large-eddy simulation of marine atmospheric boundary layers above a spectrum of moving waves. J. Atmos. Sci., 71 (11): 4001–4027, 2014.
[31]K. Yousefi, F. Veron & M. P. Buckley. Momentum flux measurements in the airflow over wind-generated surface waves. J. Fluid Mech., 895: A15, 2020.
[32]S. K. Robinson. Coherent motions in the turbulent boundary layer. Annu. Rev. Fluid Mech., 23: 601–639, 1991.
[33]M. P. Buckley & F. Veron. Structure of the airflow above surface waves. J. Phys. Oceanogr., 46 (5): 1377–1397, 2016.
[34]J. Jeong & F. Hussain. On the identification of a vortex. J. Fluid Mech., 285: 69–94, 1995.
[35]P. P. Sullivan & J. C. McWilliams. Dynamics of winds and currents coupled to surface waves. Annu. Rev. Fluid Mech., 42: 19–42, 2010.
[36]J. M. Wallace. Quadrant analysis in turbulence research: history and evolution. Annu. Rev. Fluid Mech., 48: 131–158, 2016.
[37]A.A. Grachev & C. W. Fairall. Upward momentum transfer in the marine boundary layer. J. Phys. Oceanogr., 31 (7): 1698–1711, 2001.
[38]P. P. Sullivan, J. B. Edson, T. Hristov & J. C. McWilliams. Large-eddy simulations and observations of atmospheric marine boundary layers above nonequilibrium surface waves. J. Atmos. Sci., 65 (4): 1225–1245, 2008.